RAL-TR-2001-022

THE PIN PIXEL DETECTOR - NEUTRON IMAGING

J.E. Bateman, J.F. Connolly, G.E. Derbyshire, D.M. Duxbury, A.S. Marsh, N.J. Rhodes, E.M. Schoneveld, J.E. Simmons and R. Stephenson

Rutherford Appleton Laboratory, Chilton, Didcot, Oxon, OX11 0QX, U.K.

23 April 2001

Abstract

The development and testing of a neutron gas pixel detector intended for application in neutron diffraction studies is reported. Using standard electrical connector pins as point anodes, the detector is based on a commercial 100 pin connector block. A prototype detector of aperture 25.4mm x 25.4mm has been fabricated, giving a pixel size of 2.54mm which matches well to the spatial resolution typically required in a neutron diffractometer. A 2-dimensional resistive divide readout system has been adapted to permit the imaging properties of the detector to be explored in advance of true pixel readout electronics. The timing properties of the device match well to the requirements of the ISIS pulsed neutron source.

1. Introduction

Gas avalanche counters of various types are routinely used in the construction of neutron diffractometers [1,2]. For single crystal studies with pulsed neutron sources such as ISIS it is desirable to have a detector capable of covering a useful fraction of a square meter with spatial resolution (in both dimensions) of a few millimeters with high counting rate capability and microsecond timing resolution. The advent of cheap integrated-circuit, multi-channel electronics encourages the consideration of pixellated detectors which need not suffer the readout bottle-neck experienced by the global readout of traditional 2-d gas detectors. Developed recently for x-ray diffraction applications [3,4], the pin pixel detector offers excellent potential for the construction of a pixellated neutron diffractometer detector by combining millimeter spatial resolution with excellent fast counting characteristics and the low gamma sensitivity associated with 3He gas fillings. Monte Carlo simulation of the detector predicts that with a filling of 1.5bar ^3He + 0.5bar CF_4 and a conversion depth of 30mm, a spatial resolution of 2.8mm FWHM can be achieved at the same time as a detection efficiency of 45% (for neutrons of 1Å) [5].

A prototype detector has been developed based on a standard commercial connector block containing 100 pins spaced on a pitch of 0.1 inch. Each pin functions as an independent proportional counter recording the neutron events occurring in the 2.5mmx2.5mmx30mm volume immediately above it. Operated in conformity with the conditions used in the Monte Carlo simulation detailed above, the performance of the detector was measured in tests on the ROTAX beamline of the ISIS facility at Rutherford Appleton Laboratory. In the absence of multi-channel readout electronics, a 2-D resistive-pad analogue readout was developed to permit the characterisation of the prototype detector.

2. The Pin Detector

The use of point anodes in gas counters has a long history which is well described in reference [6]. Comby and Mangeot [7] introduced a cathode focussing grid in front of an array of fine needles to make a pixel detector operating in SQS mode and capable of detecting UV-generated single electrons. Adapting this structure to linear operation with x-rays, Bateman and Connolly developed a prototype pixel detector by mounting loose connector pins in a 10 x 10 array on a 2.54mm pitch [3,4]. A serious problem with this approach was the variability of the pin dimensions which led to a rather large fluctuation in the pixel to pixel gain. The geometric precision of the 100-pin connector array solves this problem.

2.1 Design

Figure 1 shows a schematic cross-section of the present prototype pin pixel detector. The 100-pin connector array is mounted in a Macor plate which locates it and spaces it so that the anode pins are accurately positioned within the matching holes in the brass cathode (base) plate. A drift electrode consisting of aluminised mylar stretched on a GRP frame is spaced 30mm in front of the cathode plate. Electrical connection between the back of the 100 anode pins and the readout assembly is made via a

second pin array. The gold-plated brass pins of the connector array are moulded into a polyester base with great precision. A survey of the pin tips showed them to be accurately on a 2.54mm planar grid within an error of 10 microns in all three dimensions. The various layers of the anode/cathode structure are keyed together with dowels to ensure positional (and therefore gain) uniformity. Figure 2 shows the magnified appearance of a portion of the cathode as viewed from the drift space. The holes in the cathode plane are slightly counter-sunk to avoid sharp edges around the pins.

The Macor mounting electrically isolates the pin array which is maintained at earth potential while the cathode is typically held at ≈ -1300V (V_c) and the drift cathode (V_d) is held at a few hundred volts more negative than V_c. The structure of figure 1 is held in a duralumin gas-tight enclosure, which is capable of supporting an excess pressure of 1bar above ambient. Electrical sockets are provided for interface to the readout system. The gas vessel is evacuated and filled with 1.5bar of ^{3}He and 0.5bar of CF_4.

2.2 Operating Characteristics

With operating conditions V_c = -1280V and V_d = -1880V the thermal neutrons from the ROTAX beam produce the pulse height spectrum shown in figure 3 in the detector when the common cathode is connected to a charge preamplifier / main amplifier / pulse height analyser chain. The peak in the pulse height spectrum corresponding to the Q of the neutron-induced reaction (760keV) can be used to estimate the gas gain of the counter and produce the gain curve seen in figure 4.

The poor pulse height resolution of the detector is due to several factors:

(i) The ranges of the product particles of the (n,^{3}He) reaction in the counter gas are significant: 1.9mm for the triton and 6.4mm for the proton. With a detector volume of just 30mmx25mmx25mm the fraction of events in which wall losses occur is very high (≈50%). This leads to a large low energy tail to the pulse height spectrum.

(ii) The need for reasonably high drift fields in the gas mixture causes loss of charge from events shared between pins as discussed elsewhere [4].

(iii) An electron drift length of 30mm in a halocarbon gas such as CF_4 has the potential to cause significant electron attachment losses unless great care is taken with the gas purity. The pulse height spectrum of figure 3 is consistent with significant electron attachment effects.

As shown in work with x-rays, gain variation between pins is not significant (6.8% RMS). In the case of pixellated readout the poor pulse height spectrum will have little effect on the overall performance. However as will appear, in the temporary analogue readout system the need to select a band of pulse heights near the peak causes a significant loss of efficiency.

3. The Readout

The ideal readout method for the pin pixel detector is, naturally, one in which each anode is individually instrumented so that maximal benefit can be had from the rate capability of each anode. However, for test purposes (and potentially as a medium rate general purpose readout) a global analogue readout of the 25.4mm x 25.4mm tile was implemented. Since charge division electronics were available from a preceding programme [8] readout was arranged by means of a resistive pad. A readout board is coupled to the anode pin array (figure 1) in which each anode is coupled to its neighbour by a 5.1kΩ surface mount resistor. At each edge of the array a bus bar collects the charge leaving each row and column via a weighted resistor network. A charge pre-amplifier is connected to each of the four bus bars and after amplification and shaping of the pulses, the pseudo x and y co-ordinates:

$$X = \frac{(L-R)}{(L+R)} \quad \text{and} \quad Y = \frac{(T-B)}{(T+B)} \qquad (1)$$

are calculated in an analogue computer and fed to a digital data capture system. L and R represent the pulse heights available from the left and right bus bars and T and B those from the top and bottom bus bars. Tests have shown that this readout can function with excellent precision up to data rates of 400kHz in a linear readout [8]. The time constant of the anode pad readout in use with the pin array (≈1.5μs) limits this maximum rate to ≈100kHz and sets a limit of this order to the readout rate from a tile of 100 pins.

Figure 5 shows the digital image obtained from this readout when the detector is flooded with neutrons. The 100 pins are nearly all resolved with a small degree of distortion introduced by the simplified charge division algorithm. The pin matrix provides an intrinsic calibration of this distortion and facilitates off-line image rectification.

The data was captured in the ISIS data system by digitising X and Y using 6 bit ADCs and storing the counts recorded in ≈15000 time bins for each pixel within the 20ms ISIS spill time.

As with all analogue readout systems, the dynamic range of the pulses must be controlled to ensure a uniform response. In the present system this control is applied by pulse height selection of the sum of the four signals (L+R+T+B). The nature of the pulse height spectrum (figure 3) means that this restriction can result in a loss of events amounting to ≈40%.

The typical distortion of the pseudo co-ordinates is shown in figure 6 in which the average ADC pixel value of each peak in an X histogram of the data of figure 5 is plotted against the corresponding pin number. The result is a well-behaved cubic function in which the slope becomes much smaller at the edges of the field. This happens in both dimensions and results in the data in the corners being compressed in the manner shown in figure 5.

4. Imaging Performance

The spatial resolution of the detector was measured by collimating the ROTAX neutron beam to a horizontal slit of 1mm width by means of two boron carbide plates and scanning the detector vertically past the slit beam. Figure 7 shows a typical image of the slit beam as recorded by the detector. For the purposes of quantification, the image data corresponding to the central two columns (numbers 5 and 6) of pins is histogrammed vertically (Y dimension) for each exposure and the counts in each normalised to the proton beam charge (μAh) to ensure equal numbers of neutrons. Figure 8 shows the histograms from seven exposures at positions stepped by 2.5mm.

In general the slit beam shares its events between several pin rows. The histogrammed data centred on pin #5 (Y≈40) is shown with a fit to three gaussians representing the contributions of pins #4, #5 and #6. The known pin spacing (2.54mm) yields a calibration of the Y scale (0.52mm/pixel in centre field) and gives a pin resolution of σ=0.61mm (FWHM=1.44mm). The charge sharing shows that the intrinsic spatial response of the detector is wider than the readout resolution. A scan with finer resolution (0.5mm/step) shows this effect in greater detail.

Careful alignment of the slit with a pin row shows that the pin response function can be modelled well by a sum of two gaussians. Figure 9 shows the fit of the pin response function to the case in which the slit is positioned between rows 5 and 6. The small discrepancy between the fit and the data in the valley between the pins shows that there is a very small amount of interpolation, but that in general the counts are shared between the adjacent pins with little effective interpolation. Figure 10 shows a plot of the fitted counts in the contribution from each pin as the beam is scanned between the pins on a 0.5mm step. The sum of the pin contributions is also plotted and its constancy shows that no counts are lost. The few percent change in the sum is attributable to the change in sensitivity caused by the small gain variation between pins.

Since the pin (i.e. readout) resolution is better than the intrinsic detector resolution, the stepped measurements can be used as a sampling method to characterise the intrinsic detector resolution. If the five histograms taken between pin #5 and pin #6 are normalised to their individual centroids and plotted as an ensemble, the result (figure 11) gives a reasonable estimate of the intrinsic detector response. Fitting this data with a single gaussian curve gives σ = 2.1pixels = 1.09mm, or FWHM = 2.48mm.

5. Timing Performance

The time resolution of the detector is determined by two main effects: the flight time of the neutrons in the 30mm deep conversion space and the variation in the drift time of the neutron-induced electron clouds to the pins.

5.1 Flight time variation

On the ROTAX beam line the neutron has a flight path to the detector (L) of 14.91m. The detector has a depth of 30mm giving σ_L = 8.66mm (30/$\sqrt{12}$) with $\sigma_L/L = 5.8\ 10^{-4}$.

This gives a timing error proportional to the flight time (wavelength) which is, for example, 2.18μs at 1Å (t = 3757μs).

5.2 Drift time variation

The drift velocity of electrons in the current gas mixture at a drift field of 200V/cm is approximately 0.8cm/μs [9]. The 30mm drift space thus introduces a variation in the drift time of $\sigma_t = 3/(0.8x\sqrt{12}) = 1.1$μs. This variation will be further increased by a few tens of percent by the variation in rise time introduced by the random orientation of the combined track length of the proton and triton (8.3mm). The exact magnitude of the effect depends on the type of pulse discriminator used.

Thus over the region of the time of flight (TOF) spectrum of general interest, the flight time variation is the chief source of timing errors.

Figure 12 shows the TOF spectrum measured by the detector from a Mn powder sample. The data is summed over the width of a single pin column to restrict the range of scattering angle. A gaussian fit to the diffraction peak at ≈11000μs has a standard deviation of 47μs. As will be shown below, this apparent time resolution is actually wavelength spread due to the variation in scattering angle arising from the 10mm sample diameter. At t=11000μs the RMS flight time error due to the detector is 6.4μs.

6. Counting Rate Performance

The counting rate performance of the pin pixel detector was investigated by mounting it directly in the ROTAX neutron beam and varying the incident neutron rate by means of plastic beam attenuators. Fitting the standard deadtime formula to the output rates allowed the deadtimes of the various stages to be estimated. In the tests described below the incident neutron rates quoted are averages over the beam spill period of 20ms. Since the ROTAX beam is quite strongly peaked at short flight times the peak rate is rather more than a factor of two higher than the average value. As a result the system deadtimes fitted to the data are “effective” values rather than the exact instrumental values. However, they do give a useful guide to the rate performance of the detector system.

The rate performance of the detector may be considered as two distinct effects: (1) the intrinsic rate effect caused by the rate dependence of the gas gain (a feature of all gas avalanche counters) and (2) the deterioration in response associated with the particular form of electronic readout used in these tests.

6.1 The intrinsic rate performance.

Space charge effects at high counting rates can cause the gain of a pin to decrease. Tests with x-rays have shown that typically incident rates of ≈100kHz per pin are required to cause a significant (10%) decrease in the gas gain [4]. In the present tests the beam was collimated to a 1mm slit (to limit the global rate) and used to irradiate a row of 10 pins. The gain of the detector was monitored by means of an amplifier

chain and a pulse height analyser attached to the cathode electrode (figure 1). With incident neutron rates of up to 5.2kHz per pin (no absorbers in the beam) no decrease in the position of the peak in the PHA was observed. It is clear that the intensity of the ROTAX beam is not high enough to bring the pin counting rate close to the region in which gain sag may be expected.

6.2 Readout Rate Limitations

The readout system operates in three distinct blocks:

(i) The charge division network and its associated electronics, culminating in the analogue X and Y outputs from the analogue computers. To this point, the system exhibits a deadtime of 2.7μs. This is governed entirely by the slow response of the charge division network which has a risetime of ≈1.5μs.

(ii) The single channel analyser (SCA) pulse height selector. This can operate within the 2.7μs deadtime of the front-end circuits so it adds little deadtime. Its main effect is to reduce the rate by rejecting small pulses. The transmission factor is 0.57.

(iii) The analogue to digital converters (ADC) digitise the X and Y pulses with an effective deadtime of 2.3μs, which adds to the front-end deadtime.

The overall throughput of the system to final data capture may be approximated by:

$$R_{cap} = \frac{0.57 R_{inc}}{(1 + 0.006 R_{inc})}$$

where R_{inc} in the incident neutron rate on the readout and R_{cap} is the rate of data capture in the digital system (kHz). The maximum capture rate observed when the detector intercepted the (unattenuated) ROTAX beam was just over 100kHz which implies ≈500kHz for the incident neutron rate on 1 square inch of the detector.

As well as decreasing the useful efficiency of the readout, high rates lead to increasing pile-up noise in the analogue computer circuits. This eventually leads to degradation of the spatial resolution and distortion of the position signals. Figure 13 shows a series of histograms of the Y co-ordinate from digital image of flood images taken up the fifth column of pins. In these data sets the incident neutron rate on the whole detector increases from 63.8kHz to 127.4kHz. Some small distortion is visible at the edges of the field but, overall, the image of the pin column remains reasonably faithful up to the maximum rate which corresponds to a data capture rate of 41.2kHz.

Fitting a gaussian form to the fifth pin of the histogram in figure 13 shows that there is no detectable change in the width of the pin image (i.e. spatial resolution). It remains ≈1.7pixels (0.6mm) over the whole rate range.

7. Application of the Detector to Powder Diffraction

As an application of the detector which would show some of its capabilities a powder diffraction experiment was set up using a 1cm diameter cylinder of Mn powder as the sample. The detector was set up at 90 degrees to the beam direction, 90cm from the sample so that the Debye-Scherer (D-S) rings would form vertical lines on the detector. Data was acquired overnight (10.6hr). Figure 5 shows the resulting detector image summed over all TOFs (i.e. no monochromation so no structure is expected).

The TOF curves were extracted for pixels summed up each column (Y) and then the columns were summed in X to cover each pin column. (This process is not quite exact since X(x,y) and Y(x,y) are not separable functions of x and y. However, as will be seen, the loss of position accuracy (about 1mm) is small compared to the width of the D-S lines. Figure 12 shows the TOF curve for the fourth column of pins. The strongest line (at t ≈11000μs) is chosen for analysis. As shown, the peak fits well to a gaussian with a SD of 47.01μs. The Bragg condition for the first order:

$$\lambda = 2d\sin\varphi/2 \qquad (2)$$

relates the centroid of the TOF peak (i.e. wavelength λ) to the angle of the D-S line on the detector (i.e. pin no, φ) and the lattice constant d. Figure 14 shows a plot of the fitted peak centroid for each pin column against the pin number. For the small angular range involved (each pixel represents 2.78mr in angle) sin(θ) is linear with θ so a straight line is expected. This is observed. The RMS error is 2.6μs. The small "S" distortion in the data is due to the analogue readout properties.

The width of the pixel column does not define the error in the angular measurement. This is affected by such things as the finite sample size and timing errors. In order to see this effect detector images were generated in time windows which scanned across the region of the strong peak in the TOF spectrum. Starting at T=10785μs, images were generated in 8 successive windows of width 54μs. The D-S ring could now be seen crossing the detector. Since the Y dimension is uniform, and to obtain maximum statistics the pixel data was summed in Y and presented as a histogram in X.

In order to rectify the X histogram, the problem was treated as a 1-D problem. As noted above this leads to small (≈1mm) errors at the very edges of the field but this is acceptable for present purposes. The calibration curve of figure 6 and its derivative enable us to transform the dN/dX distribution to dN/dx. Figure 15 shows the resulting distribution for time slice #3. The data fits acceptably to a gaussian curve and the position (angle) can be measured with an accuracy of σ = 0.286pixels i.e. 0.80mr. The SD of the D-S ring is 2.15pixels i.e. 5.38mm or 5.98mr. The resulting FWHM of 12.7mm (14.1mr) covers most of the 25mm detector aperture, so the 2-D image is not very informative.

Since the "spiky" histograms are rather distracting to the eye, the gaussian fits of the data are presented in figure 16 to show the movement of the D-S line across the detector as the time (wavelength) slot is steadily advanced. Obviously, using the time slices centrally placed on the detector will give the maximum precision for a determination of the sample lattice constant which is found to be 2.062Å.

The contributions of the various errors to the width of the D-S line can be estimated from equation (2), which for small angles about $\varphi=90^{o}$ approximates to:

$$\Delta\lambda = d\delta\varphi/\sqrt{2} \qquad (3)$$

The relationship $t = 3758.2\lambda$ inter-converts TOF (μs) and wavelength (A). Using these relations it is found that the TOF window of 54μs gives an RMS error of 2.94mr in angle, the sample diameter (10mm) gives 3.2mr and the detector flight time variation gives 1.2mr. Combining these in quadrature gives a final SD of 4.51mr for a D-S line. This is in reasonable agreement with the value of 5.98mr observed.

8. Discussion

Within the limitations of the 2-D analogue readout system it has been possible to demonstrate the imaging and timing capabilities of the neutron pin pixel detector. The measured spatial resolution of 2.48mm FWHM matches well with the value of 2.78mm FWHM predicted by the Monte Carlo simulation [5] and the timing resolution is well matched to typical applications in neutron diffraction.

The pulse shaping time of the 2-D readout electronics was designed for an x-ray detector with significantly faster pulses. This mismatch causes considerable degradation of the pulse height spectra in the readout electronics with a resultant loss of resolution and efficiency. While pixel by pixel readout will always be superior, a resistive pad readout tailored to the neutron application may be an attractive option for a cheap though slower readout of a block of pins.

The detection efficiency has not been calibrated. For the prototype detector it will be well below the theoretical value of 45% due to the limitations of the analogue readout system. The intended pixel by pixel readout will allow the full efficiency to be recovered. The gas pressure of the prototype detector was limited simply by the vessel strength and the pin system will operate at higher gas pressures so permitting higher efficiencies if required.

The ROTAX beam is not intense enough to test the intrinsic rate limit of the detector which, it is believed, is higher than any likely to be encountered in neutron beam applications. The rate limits encountered were all properties of the resistive divide readout system. With careful setting up it is believed that data could be satisfactorily acquired at rates (per detector) of ≈100kHz, however, for full exploitation of the rate capabilities of the pin pixel detector a pixel-by-pixel readout is necessary.

References

1. S. Katano, Y. Ishii, Y. Mori, H.R. Child and J.A. Fernandez Baca, Physica B, **241-243**, (1997) 198

2. P. Convert, T. Hansen, A. Oed and J Torregrossa, Physica B, **241-243**, (1997) 195

3. J.E. Bateman and J.F. Connolly, A gas pixel detector for x-ray imaging, Proceedings of the European Workshop on X-ray Detectors for Synchrotron Radiation Sources, Aussois, France, September 30 – October 4, 1991, p92

4. J.E. Bateman, J.F. Connolly, G.E. Derbyshire, D.M. Duxbury, A.S. Marsh, J.E. Simmons and R. Stephenson, Rutherford Appleton Laboratory Report, RAL-TR-2001-009

5. J.E.Bateman, N.J. Rhodes and R. Stephenson, Rutherford Appleton Laboratory Report, RAL-TR-98-024

6. G. Comby et. al., CEN-Saclay Report DPhE/STIPE 79/01/02/36

7. G. Comby and P. Mangeot, IEEE Trans. Nucl. Sci. NS-27 (1980) 106

8. J E Bateman, J F Connolly, A B Lodge, R Stephenson, R Mutikainen, I Suni and J Morse, A gas microstrip detector for x-ray imaging with readout of the anode by resistive divide, Presented at the 5th International Conference on Position Sensitive Detectors, University College London, 13-17 September 1999

9. A. Peisert and F. Sauli, CERN Report 84-08

Figure Captions

1. A schematic cross-section of the prototype pin pixel detector showing the essential elements. The gas containment vessel is not shown.

2. A photograph of a small portion of the pin array assembly as viewed from the drift space of the detector.

3. The pulse height spectrum obtained from the common cathode of the prototype pin pixel detector when it is exposed to the ROTAX thermal neutron beam (attenuated by a 5mm Cd sheet). V_c is the cathode potential and V_d is the drift electrode potential, the pins being held at earth potential..

4. The gas gain curve derived from the peak of the pulse height spectra such as figure 3 using the Q value of the $^3He(n,p)^3H$ reaction. The drift electrode is maintained a constant 300V more negative than the cathode throughout.

5. A digital flood image (uniform illumination) of scattered neutrons as recorded by the detector under the standard operating conditions(V_c =-1280V, V_d =-1880V).

6. The non-linear response of the resistive pad readout is shown by this plot of the peak position (in ADC channels) corresponding to a given column of pins in an X histogram of the image of figure 5, summed over all Y values. The polynomial fit is used to correct the 1-D plots of the Debye-Scherer rings.

7. The digital image of the 1mm wide neutron slit beam generated by the prototype detector. The slit is approximately lined up on a row of pins.

8. A plot of the Y histograms (summed in X across the two central pin rows) obtained as the detector is traversed through the slit neutron beam in steps of 2.5mm. The scan table positions are indicated by the y values. While the data is shown for the central position, to enhance clarity only the gaussian fits for the other positions are shown.

9. A Y histogram of the digital image data when the slit beam is positioned between two columns of detector pins. The gaussian fit assumes each pin to have a response function consisting of a sum of two gaussians.

10. This plot shows the counts assigned to each pin (left and right) by the fitting process as the beam is scanned in 0.5mm steps between the pin columns. The sum of the left and right counts is also plotted.

11. An estimate of the intrinsic spatial resolution of the detector (as defined by the proton and triton ranges) is provided by normalising each of the set of histograms taken at 0.5mm steps between two pins to its mean position and fitting a gaussian to the ensemble of data points.

12. The time spectrum obtained from a single column of pins from a powder diffraction study of manganese powder. See text for details.

13. A plot of four Y histograms along pin column #5 in flood images of the ROTAX neutron beam taken at different incident rates (R_{inc}).

14. A plot of the centroid of the time spectrum of the principal diffraction line from the Mn powder sample for the summed data from each column of pins. This shows the expected (approximately) linear relation between TOF (wavelength) and pin position (angle).

15. A fit to the corrected histogram across the x dimension of the detector shows a gaussian form for the Debye-Scherer line when a narrow band of TOF (t) is selected.

16. This plot shows the expected movement of the D-S line across the detector as the selected TOF (wavelength) is increased (t_m is the centre of the 54μs TOF window for each histogram).

FIGURE 1

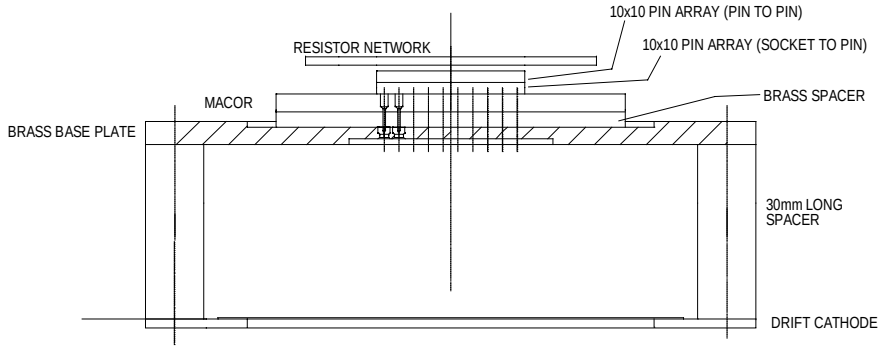

FIGURE 2

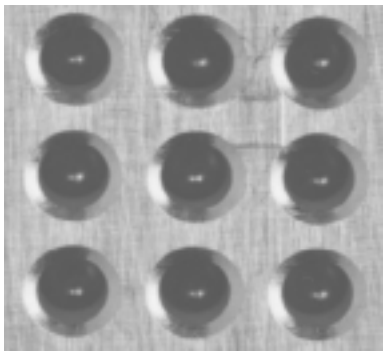

FIGURE 3

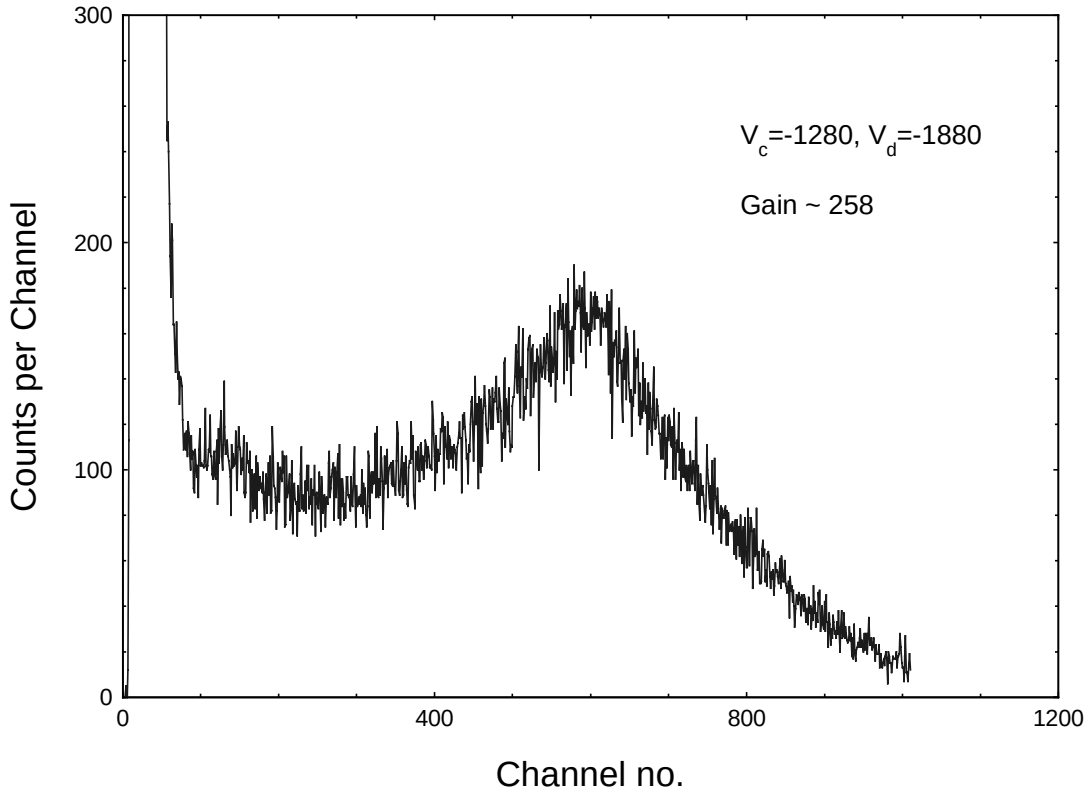

FIGURE 4

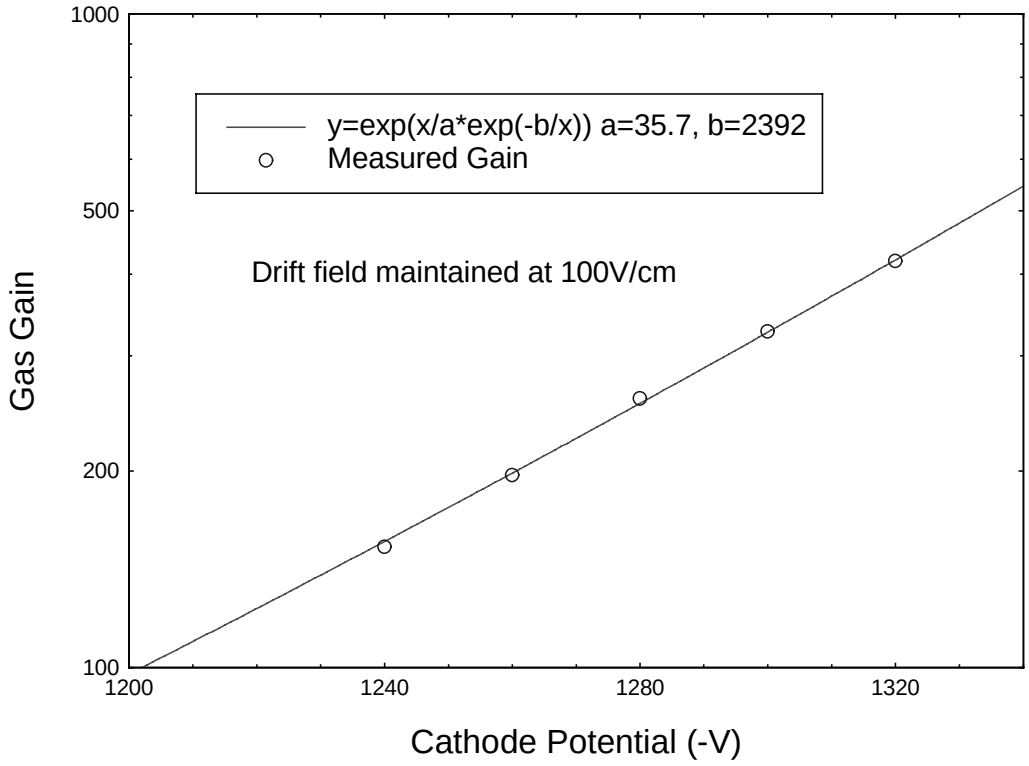

FIGURE 5

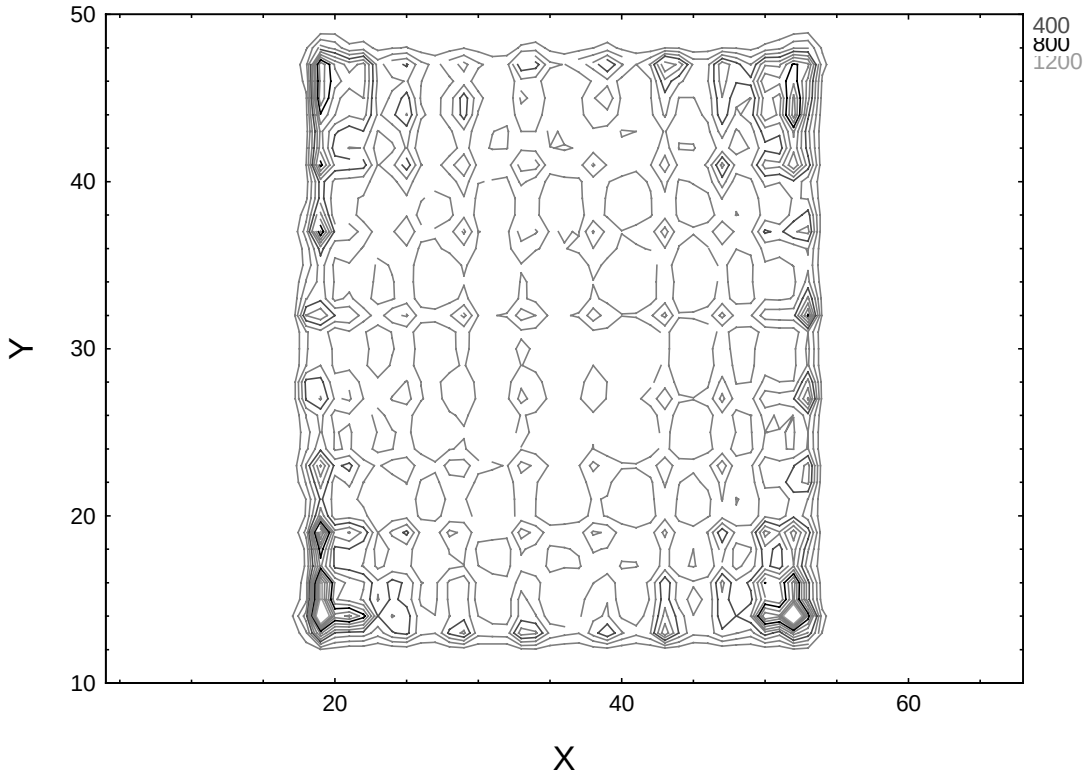

FIGURE 6

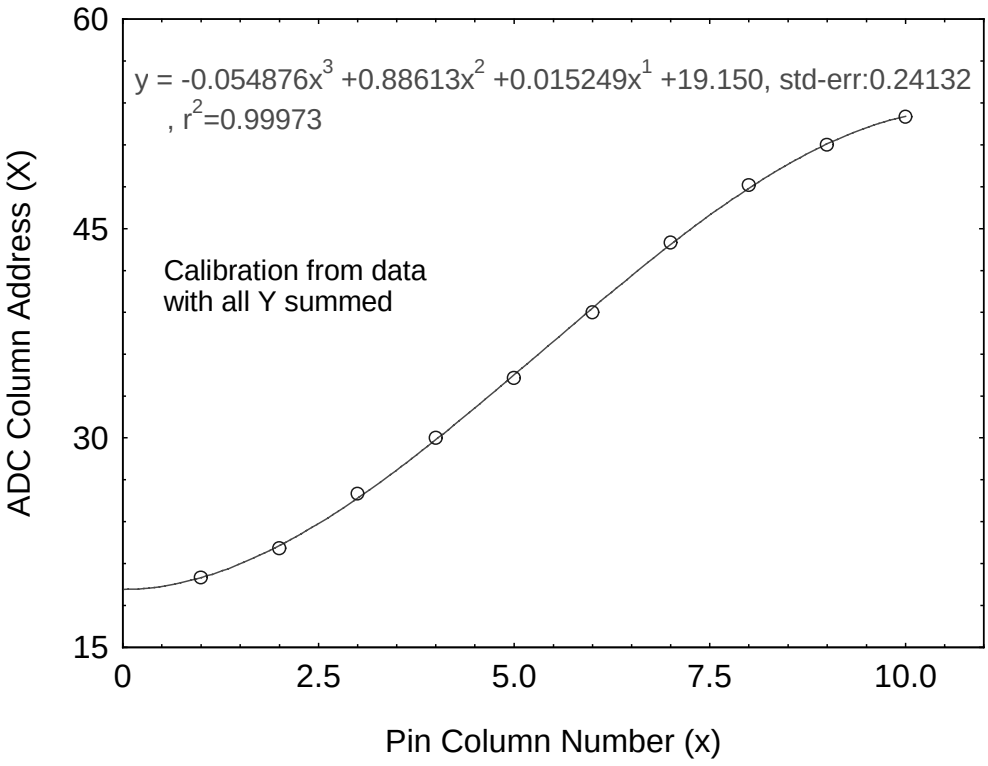

FIGURE 7

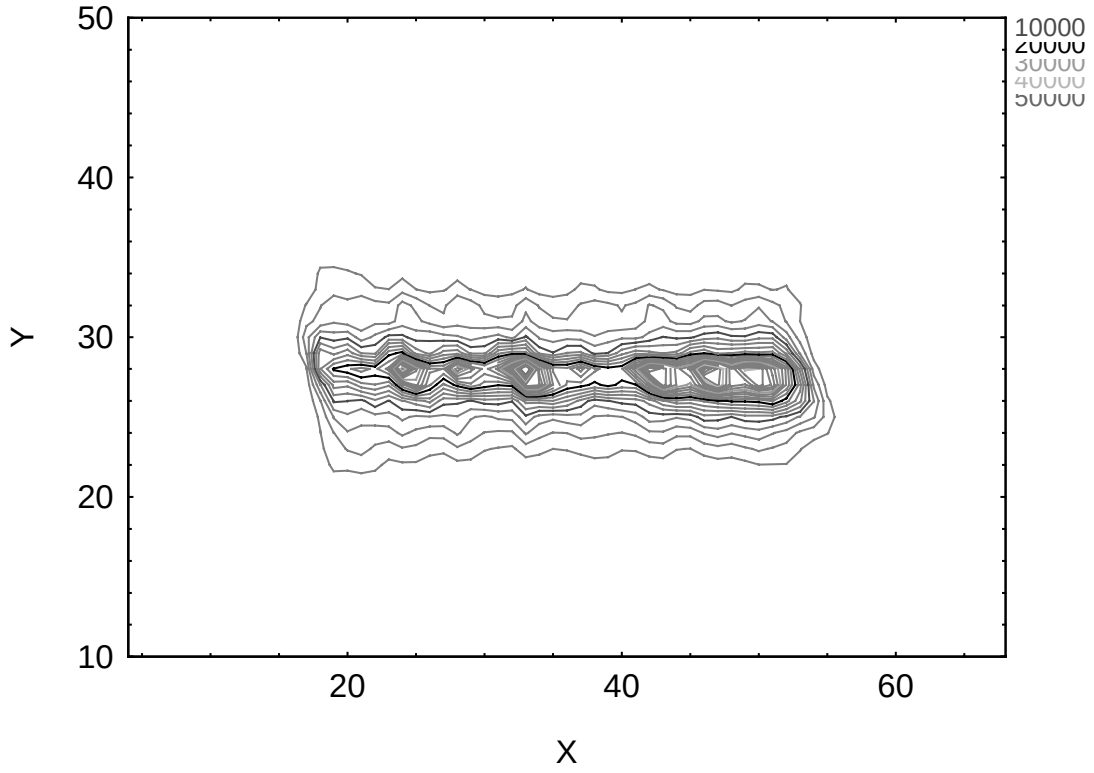

FIGURE 8

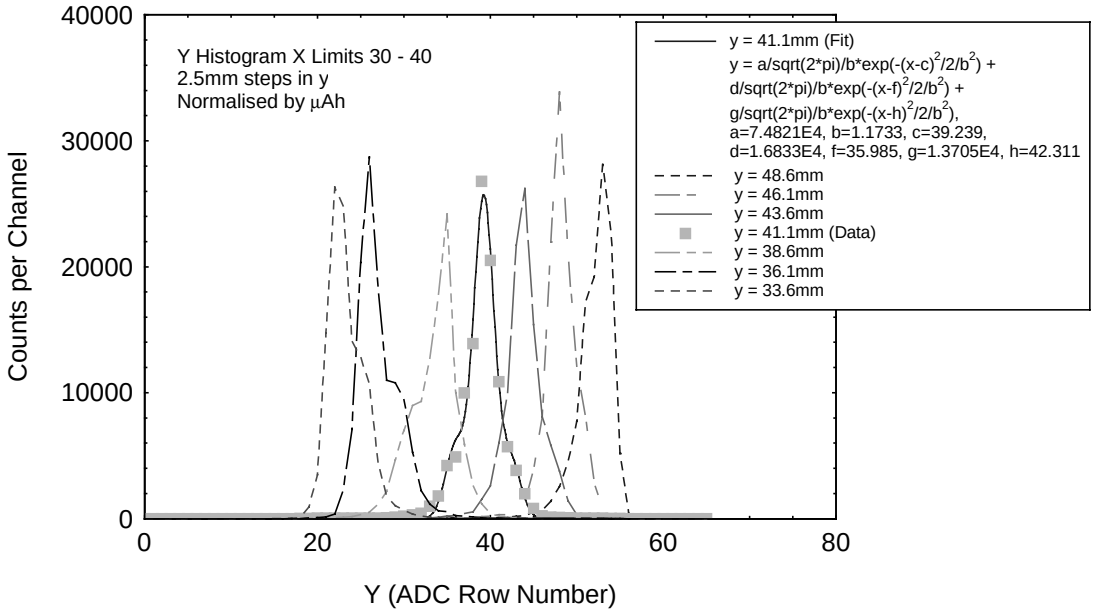

FIGURE 9

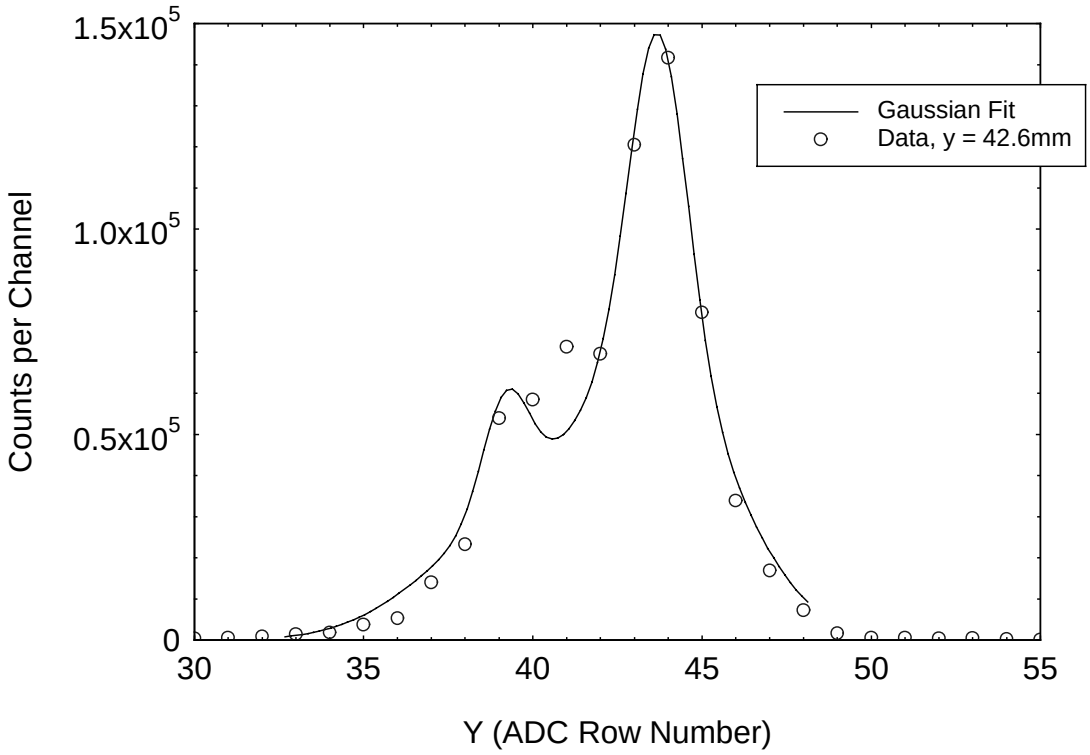

FIGURE 10

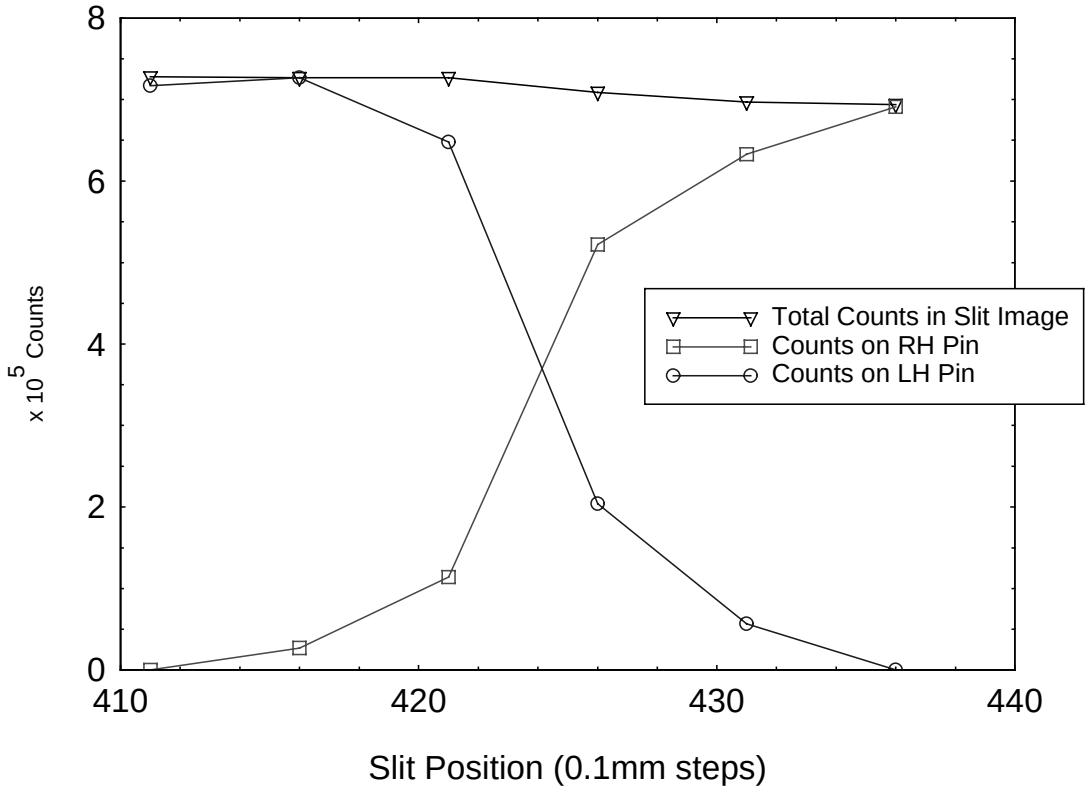

FIGURE 11

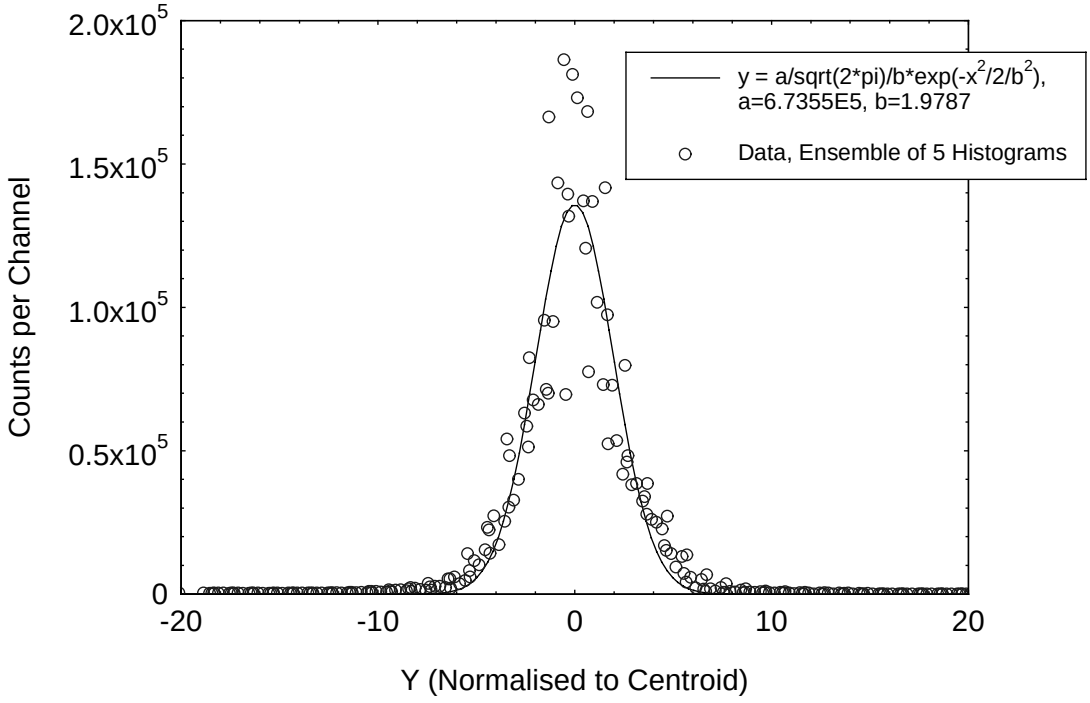

FIGURE 12

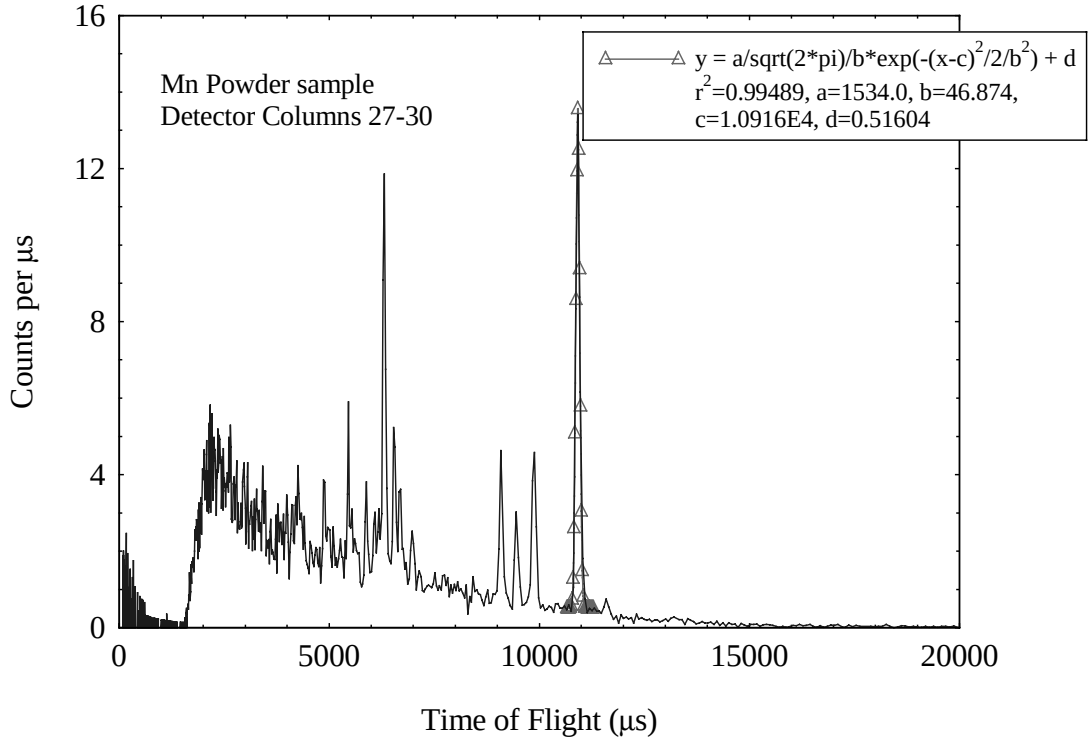

FIGURE 13

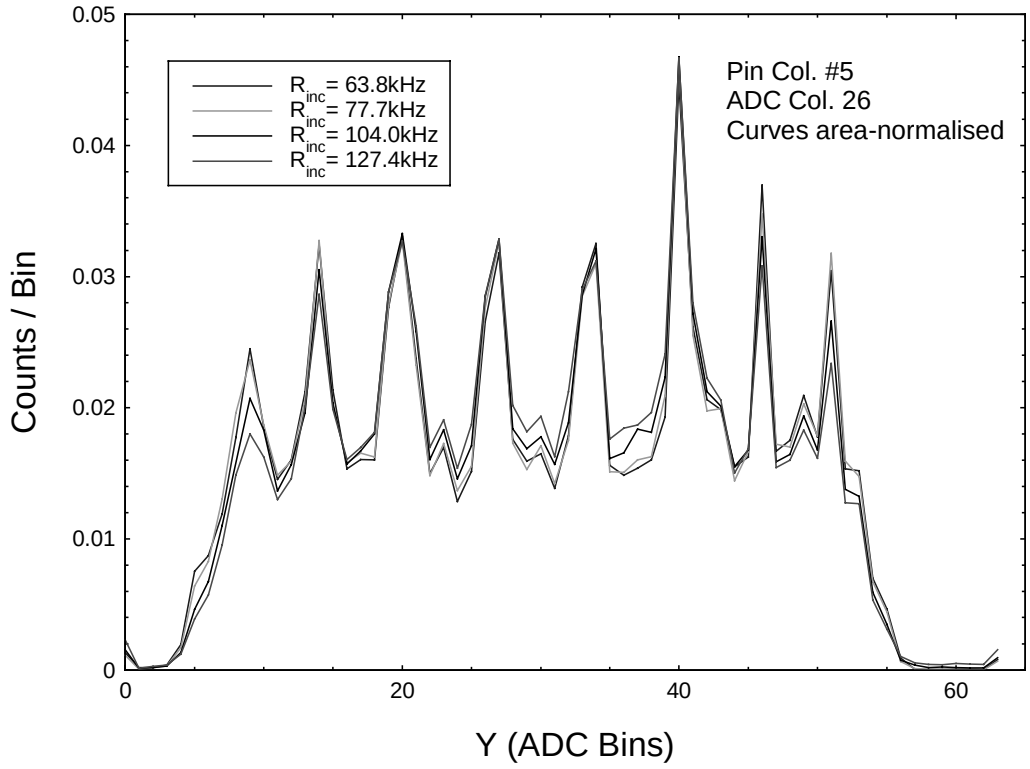

FIGURE 14

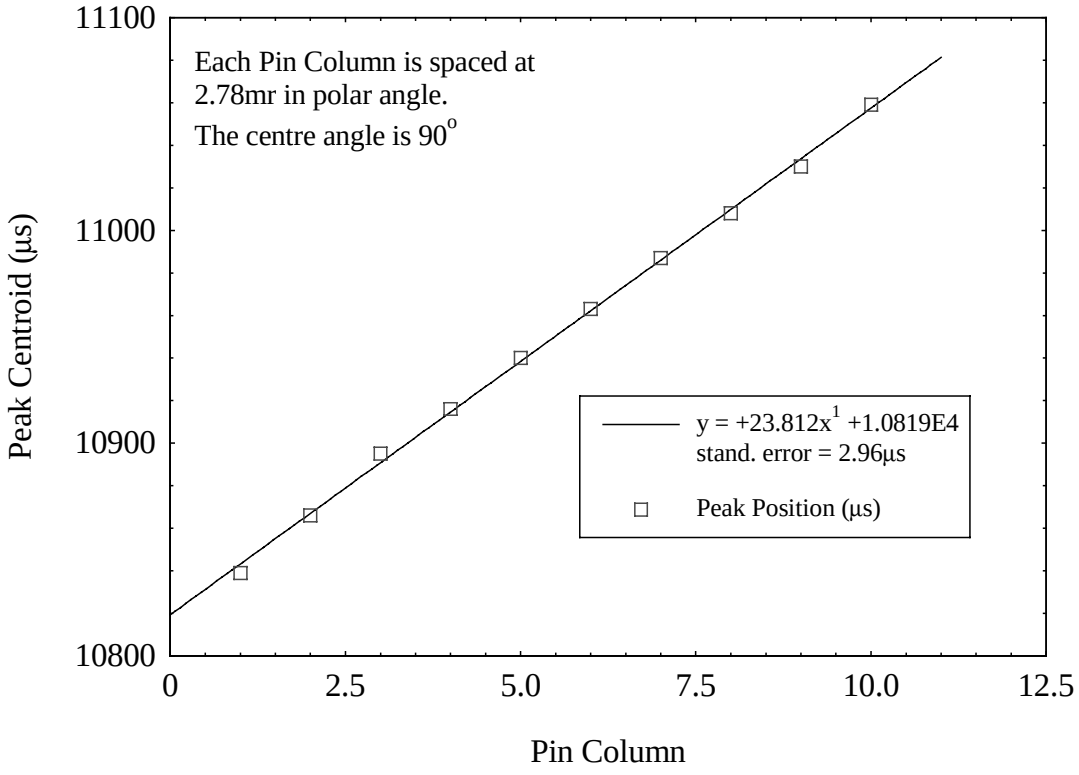

FIGURE 15

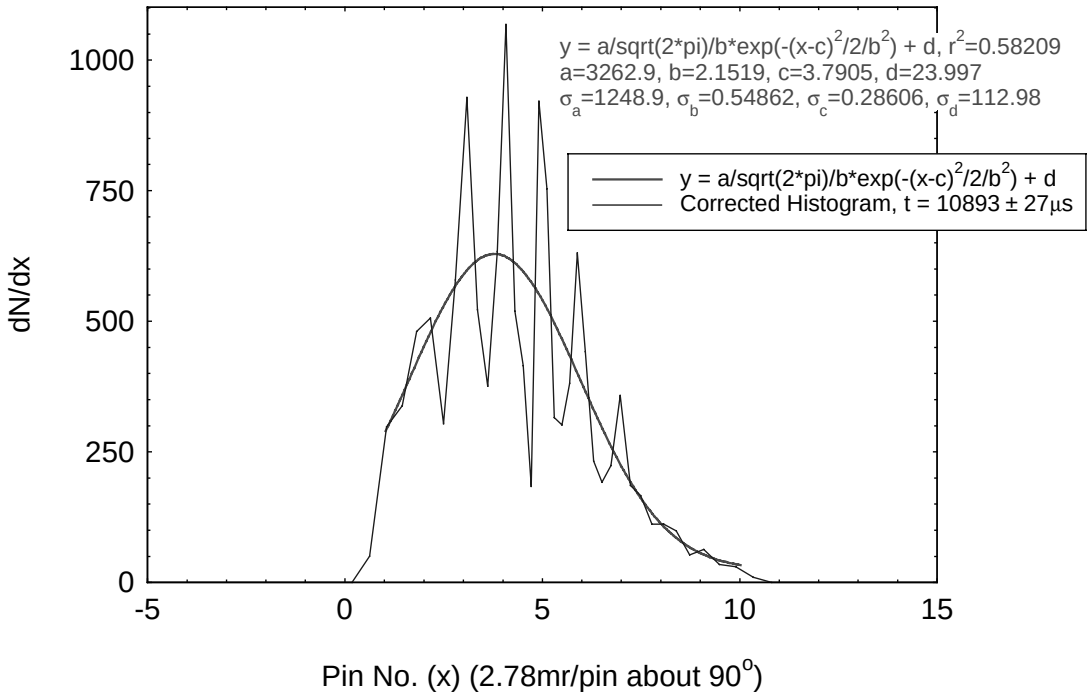

FIGURE 16